Advanced Interface Engineering in Gradient Core/Shell Quantum Dots Enables Efficient Photoelectrochemical Hydrogen Evolution

Hui Zhang, Jiabin Liu, Lucas V. Besteiro, Gurpreet S. Selopal, Zhenhuan Zhao, Shuhui Sun, and Federico Rosei**

Semiconductor core/shell quantum dots (QDs) are considered promising building blocks to fabricate photoelectrochemical (PEC) cells for the direct conversion of solar energy into hydrogen (H_2). However, the lattice mismatch between core and shell in such QDs results in undesirable defects and severe carrier recombination, limiting photo-induced carrier separation/transfer and solar-to-fuel conversion efficiency. Here, an interface engineering approach is explored to minimize the core-shell lattice mismatch in CdS/CdSe$_x$S$_{1-x}$ (x = 0.09–1) core/shell QDs (g-CSG). As a proof-of-concept, PEC cells based on g-CSG QDs yield a remarkable photocurrent density of 13.1 mA cm^{-2} under AM 1.5 G one-sun illumination (100 mW cm^{-2}), which is ≈54.1% and ≈33.7% higher compared to that in CdS/CdSe$_{0.5}$S$_{0.5}$ (g-CSA) and CdS/CdSe QDs (g-CS), respectively. Theoretical calculations and carrier dynamics confirm more efficient carrier separation and charge transfer rate in g-CSG QDs with respect to g-CSA and g-CS QDs. These results are attributed to the minimization of the core-shell lattice mismatch by the cascade gradient shell in g-CSG QDs, which modifies carrier confinement potential and reduces interfacial defects. This work provides fundamental insights into the interface engineering of core/shell QDs and may open up new avenues to boost the performance of PEC cells for H_2 evolution and other QDs-based optoelectronic devices.

1. Introduction

In the past two decades, colloidal quantum dots (QDs) have been widely studied because of their unique size/shape/composition-dependent optoelectronic properties and band alignment associated with the "quantum confinement" effect.[1] Thanks to features such as broad absorption spectra, high extinction coefficients, and the possibility of multiple exciton generation following single-photon absorption, QDs have been extensively employed as building blocks in several emerging optoelectronic technologies, such as QDs-sensitized solar cells (QDSCs),[2] QDs-based light-emitting diodes (QLEDs),[3] photodetectors,[4] temperature sensors,[5] bio-sensors,[6] luminescent solar concentrators (LSCs),[7] and photoelectrochemical (PEC) cells for hydrogen (H_2) generation from water.[1f,8] Considering the urgency of developing clean energy solutions, solar-driven PEC cells for H_2 evolution are considered auspicious means of solar-to-fuel conversion due to their ability to convert renewable and abundant solar energy into clean chemical fuel in the form of H_2.[9] H_2 is a clean and renewable fuel, which combines the advantages of high energy storage densities, cost-effectiveness, and generating water as the only byproduct of H_2 combustion.[8a] Solar-driven PEC cells provide a simple and environmentally friendly methodology for H_2 production with the potential to enable the widespread deployment of H_2 as a clean fuel.[9]

In 1972, Fujishima and Honda reported PEC water splitting to produce H_2 fuel using an n-type wide bandgap TiO_2 semiconductor as a photoanode.[10] Afterwards, metal oxide semiconductors such as TiO_2, ZnO and SnO_2 have been used extensively as photoanode materials for water splitting.[11] For instance, considerable efforts have focused on the design of these metal oxide semiconductors with 1D nanostructure morphologies such as nanorods,[12] nanotubes[13] and nanowires,[14] *etc.*, to enhance the carrier transport properties.[15] Nevertheless, the intrinsic bandgap of these semiconductors is relatively wide (>3.0 eV) and only absorbs photons in the ultraviolet range[1e,16] (representing ≈5% of the solar spectrum), yielding very low

H. Zhang, Z. Zhao
School of Advanced Materials and Nanotechnology
Xidian University
Xi'an 710126, P. R. China

J. Liu, G. S. Selopal, S. Sun, F. Rosei
Institut National de la Recherche Scientifique
Centre Énergie Matériaux Télécommunications
1650 Boulevard Lionel-Boulet, Varennes, Québec J3X 1P7, Canada
E-mail: gs.selopal@dal.ca; rosei@emt.inrs.ca

L. V. Besteiro
CINBIO
Universidade de Vigo
Vigo 36310, Spain

G. S. Selopal
Department of Engineering
Faculty of Agriculture
Dalhousie University
Truro, NS B2N 5E3, Canada

solar-to-hydrogen conversion efficiency.[17] Thanks to the broad absorption profile of QDs that overlaps significantly with the solar spectrum, they can act as effective sensitizers for TiO_2, extending the absorption range up to the visible or near-infrared range. Consequently, numerous types of bare QDs, such as PbS,[18] CdSe,[19] and $CuInSe_xS_{1-x}$,[20] have been widely used to fabricate high-performing QDs sensitized TiO_2 based PEC cells. Although the absorption limit of these photoanodes has been extended to the visible or even near-infrared regions, the photon-to-current (or fuel) conversion efficiency is still limited due to undesirable non-radiative carrier recombination events. For example, PEC cells based on bare CdSe QDs yield a comparatively low photocurrent density of ≈6 mA cm^{-2} due to the high density of surface-trap states, which act as fast non-radiative recombination centers for the photogenerated carriers.[19]

In the past few years, considerable efforts have focused on optimizing the optoelectronic properties of QD by engineering their size/shape,[18,21] irradiation with protons,[22] doping with transition metal elements,[8d,23] and designing different core/shell structures.[18,22,24] In particular, the rational design of core/shell QDs is considered promising as the core/shell architecture offers improved stability and optimized electronic band alignment compared to bare QDs.[9] Among various types of core/shell QDs, specially designed "giant" QDs (g-QDs) composed of a small-sized core covered with a relatively thick shell (several to tens of nanometers) have been widely explored to serve as light-harvesting components in optoelectronic devices.[2,3b,19,20] The absorption properties of QDs and their exciton dynamics can be controlled by adjusting the thickness, composition and the structure of the thick shell. The encapsulation of core QDs with thick shell reduces the surface traps/defects at the core surface and makes it less sensitive to the surrounding chemical conditions (ligands/solvent) due to the efficient isolation of the core from the environments.[25] As a result, core/shell g-QDs with a thick shell, in contrast to the bare QDs and thin-shell QDs (shell thickness less than 1.5 nm), exhibit significantly improved optoelectronic properties, such as superior photo-physical/chemical stability and improved quantum yield (QY).[2] However, state-of-art of core/shell g-QDs used in PEC devices still suffer from major limitations, including large lattice mismatch between core and shell materials, limited absorption range, and insufficient carrier separation/transfer at the interface. For instance, Adhikari et al. reported core/shell CdSe/CdS g-QDs with broadened absorption and improved QY compared to core QDs, resulting PEC device shows a significantly improved photocurrent density of ≈10 mA cm^{-2} and excellent durability.[19] Li et al. reported Mn-doped CuInSe/ZnSe core/shell QDs with a maximum photocurrent density of 6.0 mA cm^{-2}.[26] Guo et al. reported heavy metal-free Cu-doped $AgIn_5S_8$/ZnS core/shell QDs that show a remarkable saturated photocurrent density of 10.6 mA cm^{-2}.[27] In the abovementioned CdSe/CdS g-QDs case, the conduction band (CB) of the shell is higher than that of the core, and the valence band (VB) of the shell is lower than that of the core, allowing the formation of a physical and energy barrier potential for carrier separation and injection processes.[2,19,28] An inverted structure of CdS/CdSe g-QDs can solve this problem, yet it is still limited by the large lattice mismatch issue for application in optoelectronic devices. The large lattice mismatch in core/shell QDs results interfacial strain and thus creates defects at the sharp interface between core and shell. These defects lead to undesirable carrier recombination and further result in severe degradation of performance in core/shell QDs-based optoelectronics during device operation,[2,29] hindering their use in solar technologies. Recently, Lim et al. reported that, with the incorporation of a continuous graded $Cd_xZn_{1-x}Se$ shell in CdSe/$Cd_xZn_{1-x}Se$ core/shell QDs, the confinement potentials are "smoothened" for both electrons and holes, significantly suppressing Auger recombination.[29b] This is attributed to the interfacial gradient layer, which reduces the interfacial strain at the sharp core-shell interface caused by the lattice mismatch between core and shell materials and further modifies the carrier confinement potential. Therefore, it is desirable to design a novel structured core/shell CdS/CdSe g-QDs with a gradient interfacial layer between core and shell to solve the abovementioned shortcomings, modify the optoelectronic properties, and further explore their potential application in optoelectronic devices.

In this work, we report a systematic study of the influence of an interfacial gradient shell layer on the optoelectronic properties of CdS/$CdSe_xS_{1-x}$ core/shell g-QDs. We designed different shell structures, which allow us to compare the optoelectronic properties of a sharp core/shell interface with pure CdSe shell (denoted as g-CS), alloyed $CdSe_{0.5}S_{0.5}$ shell (denoted as g-CSA) or an interface smoothened gradient $CdSe_xS_{1-x}$ (x = 0.09–1) shell (denoted as g-CSG) by controlling the shell compositions and their ratio during the growth of each monolayer (**Figure 1**). The crystal structure of as-synthesized g-QDs was investigated by transmission electron microscopy (TEM), selected area electron diffraction (SAED), and X-ray diffraction (XRD). The optical properties of QDs reveal that g-CSA and g-CSG QDs show slightly reduced absorption limit and blue-shift PL peak position compared to the g-CS QDs. The PEC cell based on g-CSG QDs with novel gradient $CdSe_xS_{1-x}$ shell architecture yields a remarkable photocurrent density of 13.1 mA cm^{-2} under one sun illumination (AM 1.5 G, 100 mW cm^{-2}), which is ≈33.7% and 54.1% higher than that of g-CS and g-CSA QDs, respectively. Theoretical simulations indicate that the electron/hole spatial overlap decreases significantly in g-CSG QDs compared to g-CS and g-CSA QDs, which facilitates carrier separation and transfer at the QDs/TiO_2 interface. Carrier dynamics measurements demonstrate that g-CSG QDs with continuous gradient $CdSe_xS_{1-x}$ shell architecture show a significantly improved carrier transfer rate, prolonged electron lifetime and reduced charge transfer resistance, thanks to the unique gradient $CdSe_xS_{1-x}$ shell structure. This work shows that interface engineering of core/shell QDs yields high-performance PEC cells for H_2 evolution and can be extended to fabricate other QDs-based optoelectronic devices such as QDSCs, QLEDs and LSCs.

2. Results and Discussion

2.1. Synthesis and Structural Characterization

First, core CdS QDs were synthesized via a simple, well-known hot injection method. The obtained core CdS QDs were subsequently used as seeds to grow the shell layers to form core/shell g-QDs. To precisely control the shell compositions, we used successive ionic layer adsorption and reaction (SILAR) for the synthesis of three types of core/shell g-QDs. As shown in

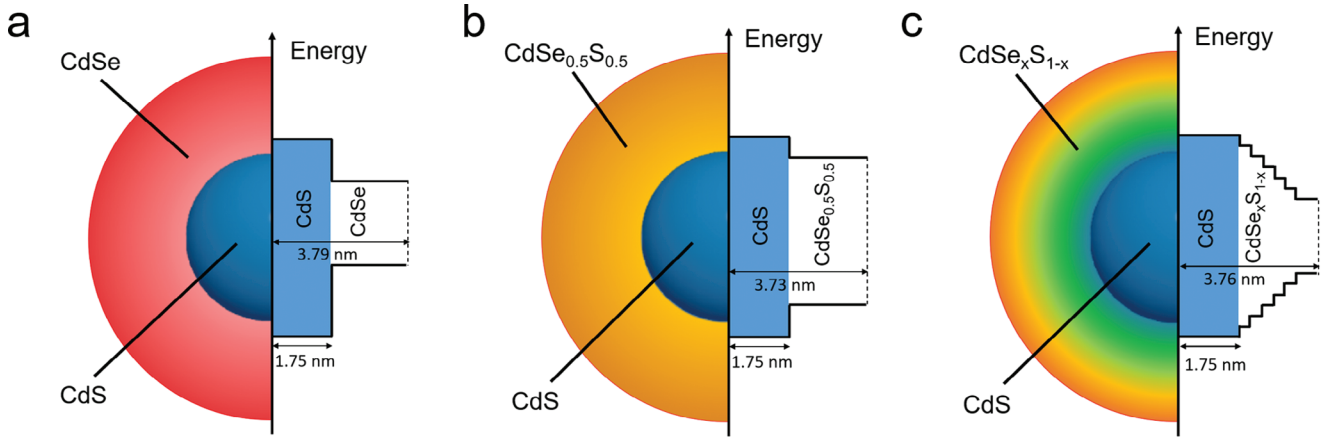

Figure 1. Schematic illustration of the as-synthesized core/shell g-QDs with different shell combined compositions and approximate band alignment structures for a) g-CS, b) g-CSA, and c) g-CSG QDs, respectively.

Figure 2a, six SILAR cycles of CdSe shell were overgrown at 220°C to form g-CS QDs. Six SILAR cycles of $CdSe_{0.5}S_{0.5}$ shell (the Cd/S/Se precursor was set as 1:0.5:0.5 by molar) were overgrown to form g-CSA QDs. Six SILAR cycles of $CdSe_xS_{1-x}$ shell [the Cd/Se/S precursor was set as 1:x:(1-x) by molar, x value varying from 1/11 to 1] were overgrown to form g-CSG QDs. The details are reported in the *Experimental Section*. The as-synthesized QDs were then purified twice using ethanol and re-dispersed in toluene for further characterization and the fabrication of PEC devices.

The size of CdS core QDs is about 3.50 ± 0.30 nm in diameter (D), as evidenced by TEM images of the as-synthesized core CdS QDs in Figure 2b. A high-resolution TEM (HR-TEM) image of the core CdS QDs in the inset of Figure 2b confirms the crystal plane d-spacing of 0.32 nm, corresponding to the (1 0 1) plane of hexagonal wurtzite (WZ) CdS. Figure S1a (Supporting Information) shows the SAED patterns of the core CdS QDs with interplanar spacing values of 3.55, 3.36, 3.15, 2.06 and 1.75 Å, which is consistent with the crystal lattice planes (1 0 0), (0 0 2), (1 0 1), (1 1 0), and (1 1 2) of WZ CdS.[30]

Representative bright field TEM images (Figure 2c–e) show that the as-synthesized core/shell g-QDs have a narrow size distribution after the growth of the different designed shell layers. The average sizes of core/shell g-QDs are summarized in **Table 1**, showing diameters of 7.58 ± 0.56 nm for g-CS, 7.46 ± 0.55 nm for g-CSA and 7.52 ± 0.50 nm for g-CSG QDs, as confirmed by TEM images and measured size distributions (Figure S2, Supporting Information). The crystal plane d-spacing in the insets of Figure 2c–e is calculated to be ≈3.7 Å and ≈3.5 Å with an angle of 90°, which corresponds to the (100) and (002) plane of the WZ crystal structure of CdSe. Both SAED and HR-TEM images reveal the appearance of the WZ phase after shell growth. The SAED patterns in Figure 2f and Figure S1b,c (Supporting Information) confirm the formation of the hexagonal WZ phase after shell growth. The distances of interplanar spacing are 0.371, 0.350, 0.329, 0.215, 0.201, and 0.180 nm, which are indexed to the lattice planes of (100), (002), (101), (110), (103), and (112), respectively, of WZ CdSe.[30] The result confirms that, after the growth of the shell, all core/shell g-QDs present the shell formation of a WZ structure. It is difficult to distinguish the core/shell interface and differences in the interplanar distance by HR-TEM imaging due to the small QDs size.[31]

Table 1. Structural and optical properties of the as-synthesized core CdS, core/shell g-CS, g-CSA and g-CSG QDs dispersed in toluene.

QDs	[a)R] [nm]	[a)D] [nm]	[b)H] [nm]	Absorption peak [nm]	PL peak [nm]	Lifetime [ns]	QY [%]
CdS	1.75 ± 0.15	3.50 ± 0.30	0	432	441	35 ± 3	7 ± 1
g-CS	1.75 ± 0.15	7.58 ± 0.56	2.04	617	649	13 ± 1	8 ± 1
g-CSA	1.75 ± 0.15	7.46 ± 0.55	1.98	593	632	19 ± 2	12 ± 1
g-CSG	1.75 ± 0.15	7.52 ± 0.50	2.01	591	631	19 ± 2	25 ± 2

[a)] R is the CdS core radius, [a]D is the QDs diameter and; [b)] H is the shell thickness.

We followed the variation of the elemental composition of the core CdS QDs and these core/shell g-QDs with the X-ray photoelectron spectroscopy (XPS) surface analysis technique. High-resolution XPS spectra in small energy regions around the expected peak positions of each element are also shown in Figure 2g. Here, the binding energies obtained from the XPS analysis have been calibrated by referencing the C 1s peak to 284.8 eV. As shown in Figure 2g (left), the spectra for Cd 3d can be resolved into $3d_{3/2}$ and $3d_{5/2}$ peaks at 411.8 and 405.0 eV for all the samples, respectively. These energy positions are consistent with the reported XPS spectrum of Cd.[32] Similarly, as shown in Figure 2g (middle), for all the core/shell g-QDs, the XPS spectra in the range from 155 to 170 eV can be resolved into four peaks of Se $3p_{3/2}$, S $2p_{3/2}$, S $2p_{1/2}$, and Se $3p_{1/2}$ at ≈160.0 eV, 161.4 eV, 162.5 eV and 165.8 eV, respectively.[32–33] For core CdS QDs, only two peaks at 161.4 eV and 162.5 eV in this energy range correspond to S $2p_{3/2}$ and S $2p_{1/2}$ peaks. This implies the presence of S in all samples and Se only in the g-CS, g-CSA and g-CSG core/shell QDs. However, the intensity ratio of Se/S in g-CS QDs was detected to be weaker compared to that of g-CSA and g-CSG QDs due to the former one being designed with more Se at the QDs surface and the latter two with less Se. Besides, Figure 2g (right) shows the high-resolution XPS spectra of Se 3d. We observe a peak for Se $3d_{5/2}$ at the binding energy of 54.0 eV for all the core/shell g-QDs,

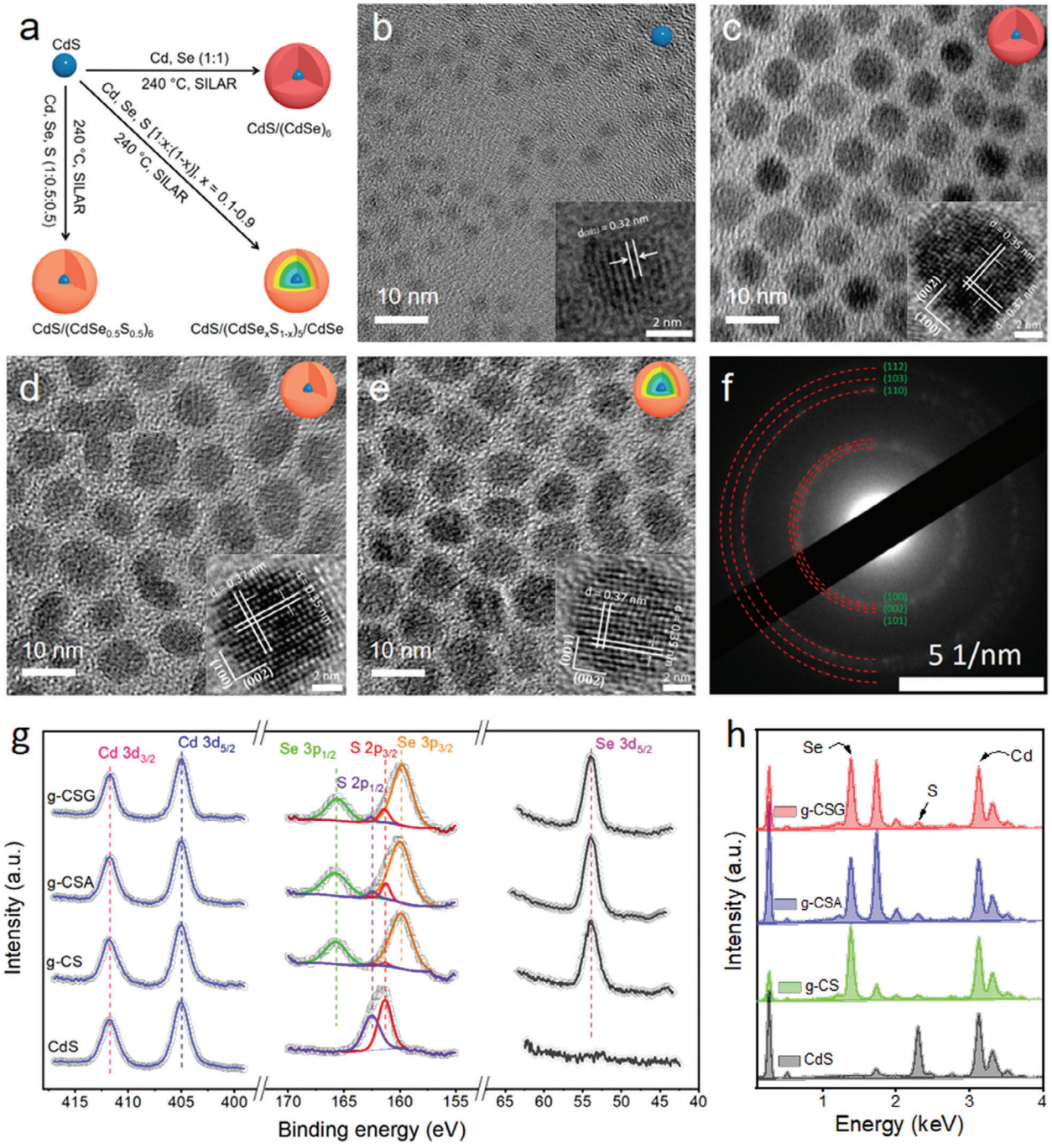

Figure 2. a) Schematic illustration of the synthesis of core/shell g-QDs with different shell compositions and structures. Representative bright field TEM images of b) CdS, c) g-CS, d) g-CSA, and e) g-CSG QDs. The insets show the corresponding HR-TEM images. f) SAED pattern of g-CSG QDs showing the d-spacing of crystal planes. g) High-resolution XPS spectra of elemental Cd $3d_{3/2}$ and $3d_{5/2}$ (left), S $2p_{3/2}$ and $2p_{1/2}$ (Se $3p_{3/2}$ and $3p_{1/2}$) (middle) and Se $3d_{5/2}$ (right) for the core/shell g-QDs. h) EDS spectra of CdS, g-CS, g-CSA and g-CSG QDs, respectively.

assigning to the characteristic spectra of Se.[34] However, in the spectrum of core CdS QDs, there is no Se peak occurring in this energy range. In summary, XPS analysis confirms the elemental composition discrepancy in all designed QDs, which is consistent with the addition of precursors in different QDs during SILAR.

The XRD was employed to characterize the crystal structures of as-synthesized QDs. As shown in Figure S3 (Supporting Information), XRD peaks for core CdS QDs are broad with discernible shoulders between 23 to 30 degrees, consistent with the lattice planes of (1 0 0), (0 0 2), and (1 0 1) for WZ CdS (JCPDS No. 00-001-0780). The other two peaks occur at 43.9 and 51.8 degrees

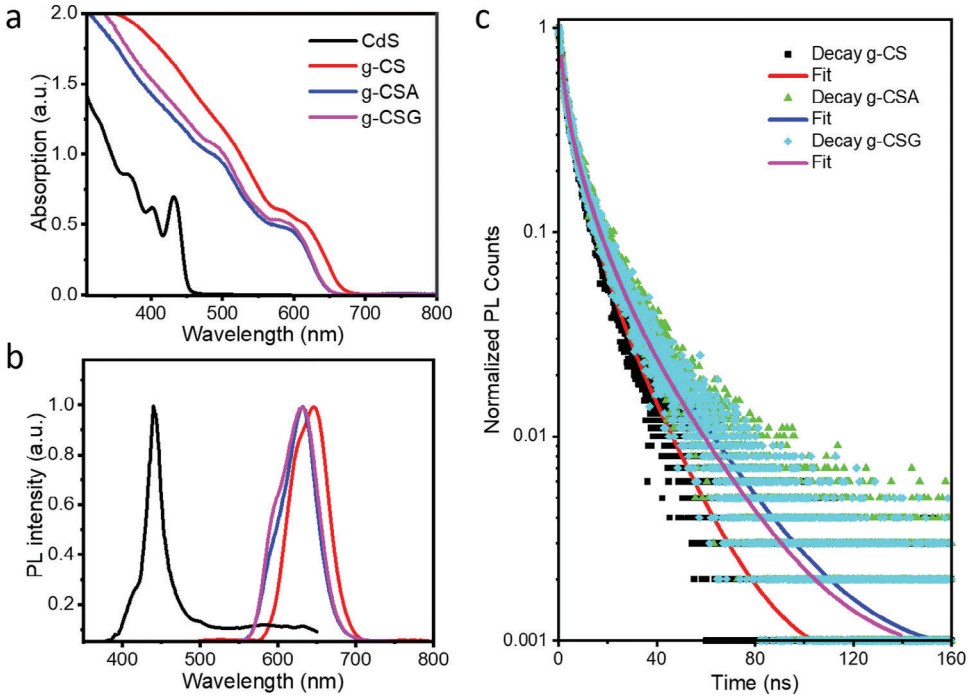

Figure 3. Optical properties of the as-synthesized CdS, g-CS, g-CSA and g-CSG QDs in toluene: a) absorption and b) PL spectra. The excitation wavelength is $\lambda_{ex} = 350$ nm for core CdS QDs and $\lambda_{ex} = 500$ nm for core/shell g-QDs samples. c) Transient PL spectra of heterostructured g-CS (black dots), g-CSA (green dots) and g-CSG (cyan dots) QDs in toluene, respectively. The fitted curves are shown in red, blue, and magenta lines, respectively. The excitation wavelength is $\lambda_{ex} = 444$ nm for core/shell g-QDs samples.

for the XRD pattern of core CdS QDs, corresponding to the lattice planes of (1 1 0) and (1 1 2) for CdS. After shell growth over the CdS core, the XRD peaks for core/shell g-QDs are broad with discernible shoulders between 22 to 29 degrees, consistent with the lattice planes of (1 0 0), (0 0 2), and (1 0 1) for hexagonal WZ crystal structure of CdSe (JCPDS No. 00-002-0330). The other characteristic peaks of core/shell g-QDs appear at 35.1, 42.2, 45.6, and 49.7 degrees, which are indexed to the lattice planes of (102), (110), (103), and (112) for a WZ CdSe. As discussed above, we find that the three peaks at the lowest angles in the diffraction patterns are not well separated because these three peaks originate from the lattice planes of (100), (002), and (101) of WZ CdSe tend to merge into one peak in the XRD pattern. Nonetheless, the XRD peaks show a slight shift (≈ 0.35 degrees) toward the larger degree for g-CSA and g-CSG QDs with respect to g-CS QDs, which is attributed to the alloying of the shell. This is due to the broader diffraction peak caused by the small size of QDs compared to the "bulk" materials, as well as their peak positions are very close. However, "shoulder" peaks originating from WZ phase signals can still be slightly observed. These results are consistent with SAED patterns. Previous reports also described a similar growth behavior for an inverted structure of core/shell CdSe/CdS QDs, in which the crystalline phase of the shell is dictated by the crystal structure of the core.[30]

As shown in Figure 2h, energy dispersive X-ray spectroscopy (EDS) spectra show characteristic peaks originating from Cd, S in bare CdS QDs and Cd, S, Se peaks in core/shell g-QDs. The EDS spectra further confirm the presence of elemental Cd and S in core CdS QDs and elemental Cd, Se and S in each core/shell g-QDs, in agreement with the XPS results.

2.2. Optical Characterizations

The optical properties of as-synthesized QDs were investigated using absorption and PL spectroscopy in toluene and at room temperature. The normalized absorption and PL spectra of as-synthesized core CdS and core/shell g-QDs are shown in **Figure** 3a,b and the calculated optical parameters of the corresponding g-QDs are reported in Table 1. As seen in Figure 3a,b, the CdS QDs show a first-excitonic absorption peak at ≈432 nm and a PL peak at 441 nm. For g-CS QDs, the absorption is broader than core CdS QDs and the absorption peak shifts from 432 to 617 nm, which is attributed to the growth of a smaller band gap CdSe shell over larger band gap CdS core QDs. For the alloyed or gradient shell samples of g-CSA or g-CSG, the first-excitonic absorption peak reveals a systematically slight blue shift compared to that of g-CS due to the reduced amount of Se in the shell layers. The alloyed shell g-CSA and gradient shell g-CSG QDs show first-excitonic absorption peaks at 593 and 591 nm, respectively. The PL spectrum of as-synthesized g-CS shows a PL peak at 649 nm. The PL peaks of as-synthesized g-CSA and g-CSG QDs are observed at 632 and 631 nm, respectively, showing a systematic blue shift toward a shorter wavelength. This is consistent with the trend observed in the absorption spectra.

To better understand the role of different shell compositions and structures on the carrier dynamics in QDs, we studied the transient PL spectra of core/shell g-QDs. The transient PL spectrum of QDs reveals different relaxation processes of photoexcited electrons. The ensembles of QDs usually lead to multiexponential PL decay profiles because of the sample inhomogeneities

(e.g., size, surface and shape).[35] The PL decay curves are fitted by three-exponential equation as follows:

$$I(t) = a_1 e^{\left(-\frac{t}{\tau_1}\right)} + a_2 e^{\left(-\frac{t}{\tau_2}\right)} + a_3 e^{\left(-\frac{t}{\tau_3}\right)} \quad (1)$$

The intensity-weighted average lifetime (τ) is calculated from transient PL fitting results using the following equation:[36]

$$\tau = \frac{\sum a_i \tau_i^2}{\sum a_i \tau_i} \quad (2)$$

where a_i (i = 1, 2, 3...) are the coefficients of the fitting of PL decay and τ_i (i = 1, 2, 3...) are the characteristic lifetimes, respectively. Figure S4 (Supporting Information) shows the PL decay dynamics of bare CdS QDs with a lifetime of 35 ns. The PL decay dynamics measurements and fitting results in Figure 3c of the g-CS (black dots and red line), g-CSA (green dots and blue line) and g-CSG (cyan dots and magenta line) QDs show a lifetime of 13, 19, and 19 ns, respectively. The fitting parameters of various types of QDs are shown in Table S1 (Supporting Information). The shorter characteristic lifetime of τ_1 can be typically attributed to the recombination of intrinsic excitons,[37] while the middle and longer lifetimes (τ_2 and τ_3) might be associated with the involvement of surface trap states in the carrier recombination process.[38] These trap states exhibit a complex energy distribution and thus are differentiated into two groups.[39] The lifetimes of QDs after shell growth evidently decrease with respect to bare CdS QDs. This is due to the strong electron leakage into the shell in inverted type I core/shell g-QDs compared to bare QDs, rendering electrons in these core/shell g-QDs sensitive to the surface traps.[25c,40] The measured lifetime values for g-CSA and g-CSG QDs are around 1.5 times longer than that for g-CS QDs. This may be attributed to the lower core/shell lattice mismatch and interface strain in g-CSA and g-CSG QDs, reducing the electron/hole recombination on the interface.

The longer PL lifetime in CdS QDs compared to that in all the core/shell QDs may also be attributed to the difference in emission mechanism/carrier recombination process between them. For CdS core QDs, the emission process involves the band edges of CdS and trap states. For the case of the as-prepared core/shell QDs, the emission process involves the band edges of shell and trap states due to their inverted type I band alignment. Several studies reported average lifetime values of ≈ 42.0, 34.4, and 36.6 ns for CdS QDs,[41] while the average lifetime values of CdSe QDs in previous work were reported as ≈ 20.0 and 16.5 ns, respectively.[19,42] These values are comparable with the results of CdS and core/shell QDs in this work.

The typical QYs of bare CdS, g-CS, g-CSA, and g-CSG QDs in toluene are ≈7%, 8%, 12%, and 25%, respectively, as reported in Table 1. The g-CS and g-CSA QDs present a larger core/shell lattice mismatch, inducing many interfacial defects, which act as carrier recombination centers. These recombination centers lead to non-radiative decay events, resulting in lower QYs in g-CS and g-CSA QDs compared to g-CSG QDs. It is particularly interesting that the QY of g-CSG QDs is ≈25%, showing a noticeable increase, which is about three times higher than that of g-CS QDs and about two times higher than that of g-CSA QDs. This is attributed to the reduced carrier recombination in g-CSG QDs because the cascade gradient shell modifies the carrier confinement potential and reduces interfacial defects.[29b]

2.3. Photoanode Characterization

Figure 4a shows a schematic illustration of the as-prepared photoanode architecture, which is composed of a fluorine-doped tin oxide (FTO)-coated glass substrate, a compact TiO_2 blocking layer and QDs-sensitized mesoporous TiO_2 film. Figure 4b,c shows the morphological characterization of the bright field TEM image for the cross-sectional FTO-coated glass substrate after spin-coating a thin, dense and pinhole-free TiO_2 blocking layer on top. The detailed discussion on TiO_2 film is reported in the Supporting Information.

After QDs synthesis and TiO_2 film preparation, as-synthesized QDs were used to sensitize the TiO_2 mesoporous film by electrophoretic deposition (EPD). To investigate the uniformity of QDs distribution inside the TiO_2 mesoporous film after EPD, SEM and EDS measurements were carried out on the cross-section of the photoanode. Figure 4d shows a representative SEM image of the cross-sectional QDs-sensitized TiO_2 photoanode. The total thickness of TiO_2 mesoporous film was measured at ≈ 12 μm in the SEM image, which is consistent with the results measured by contact profilometry. Figure 4e reports the EDS line mapping presenting the relative weight ratio of different elements along the direction of the white arrow in Figure 4d, which comprises both the glass/FTO (initial ≈ 1.4 μm) and TiO_2 film (remaining ≈ 12.0 μm). This result demonstrates that the QDs are homogeneously distributed inside the TiO_2 mesoporous film, resulting in the formation of high-quality TiO_2/QDs photoanode after EPD. Figure 4f–m display the EDS 2D mapping images of different element distributions of C (red), Na (blue), Si (cyan), Sn (yellow), Ti (pink), Cd (orange), S (green), and Se (purple) in the film, respectively. The signals corresponding to elemental C, Na and Si are attributed to the glass substrate. The signals of elemental Sn and Ti originate from FTO and TiO_2, respectively. Elemental Cd, S and Se from QDs are also clearly observed in the mapping images, suggesting a uniform distribution of colloidal QDs in the TiO_2 mesoporous film. Furthermore, the TEM image of QDs adhering on mesoporous TiO_2 in Figure 4n also proved the homogenous distribution of QDs on the surface of TiO_2 nanoparticles. As shown in the yellow dotted circle of Figure 4n, QD particles are observed on the surface of TiO_2 particles homogeneously. This indicates that the high dispersion of QDs is not damaged during the EPD process, confirming the formation of a high-quality photoanode. As shown in Figure 4o, the EDS spectrum of QDs sensitized TiO_2 mesoporous film confirms the presence of Ti, O, Cd, Se and S in the photoanode. The signals of C and Cu originate from the TEM sample grid.

2.4. PEC Performance

As proof-of-concept, three different kinds of as-synthesized g-QDs sensitized TiO_2 photoanodes were employed as sunlight harvesting components in PEC devices. Before device fabrication, two cycles of cetyl-trimethyl ammonium bromide (CTAB) ligand exchange treatment were applied on the photoanodes to

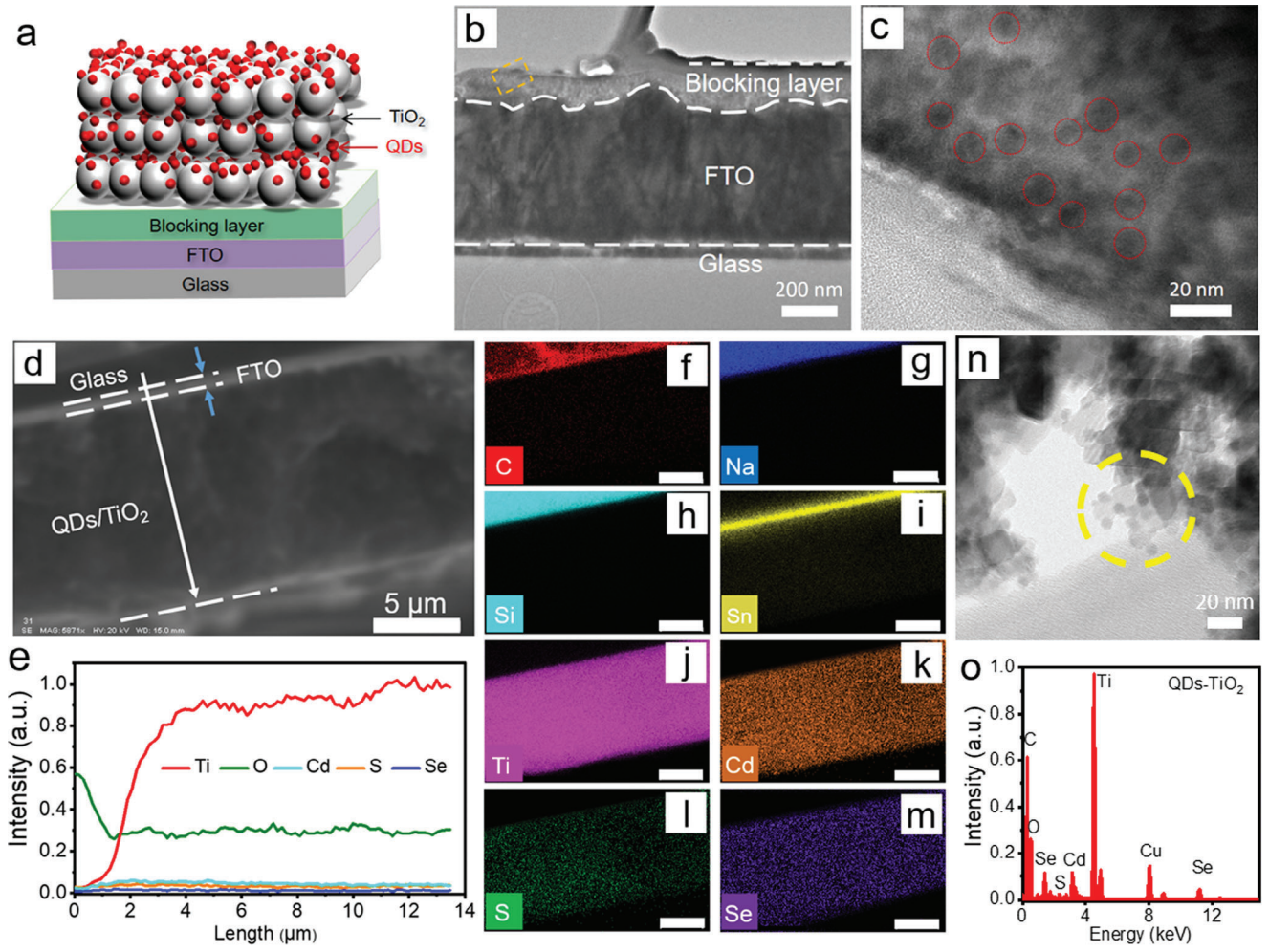

Figure 4. a) The schematic illustration of the glass/FTO/blocking layer/QDs-TiO_2 photoanode architecture. Morphological characterization of the cross-sectional FTO-coated glass substrate with a thin TiO_2 blocking layer on top: b) TEM image and c) HR-TEM image by observing the yellow rectangle area in (b). The different sections are shown by dashed lines in (b). d) Representative cross-sectional SEM image of as-fabricated g-CSG QDs/TiO_2 photoanode. The different sections are distinguished using dashed lines in (d). e) EDS line mapping of different elements as the direction of the white arrow in the image (d). (f–m) The corresponding EDS 2D mapping for element distributions of f) C (red), g) Na (blue), h) Si (cyan), i) Sn (yellow), j) Ti (pink), k) Cd (orange), l) S (green), and m) Se (purple) in the photoanode, respectively. n) TEM image of QDs adhered to TiO_2 film after EPD. The presence of QDs can be evidently distinguished in the region of the dotted yellow circle. o) EDS spectrum of QDs on TiO_2 acquired from the area in image (n).

replace the long-chain oleic acid (OAc) ligands with short-chain Br^- ligands, which can maintain high carrier mobility while reducing defect density.[43] This strategy is known to be favorable for reducing losses from recombination and improving the stability of PEC cells.[19] Additionally, it is reported that ZnS coating layers can significantly protect the QDs from photocorrosion.[19] Therefore, two SILAR cycles of the ZnS passivation layer were performed before the PEC performance measurements to inhibit photocorrosion.

The PEC performance was assessed using a traditional three-electrode configuration consisting of a g-QDs sensitized TiO_2 film as working electrode, Ag/AgCl as reference electrode and a platinum (Pt) foil as counter electrode. The measurement was conducted at room temperature (25 °C), by using an electrochemical workstation. The simulated one sun illumination was settled as AM 1.5 G with an intensity of 100 mW cm^{-2}. **Figure** 5a shows the schematic diagram of PEC cells with as-synthesized g-CSG QDs as light-harvesting components. Typically, electron-hole pairs (excitons) are generated under one sun illumination, when the QDs absorb sunlight with energy higher than their bandgap. The photo-excited electrons then leak from the core to the shell region, followed by dissociation at the QDs/TiO_2 interface. The electrons in the CB of the QDs are injected into the CB of TiO_2 mesoporous film due to the favorable band alignment. Subsequently, the electrons are collected by the FTO film and transferred to the Pt counter electrode through the external circuit, followed by the H_2 evolution reaction that takes place on the surface of Pt. The electrolyte contains 0.25 M Na_2S and 0.35 M Na_2SO_3 (pH = 12.5), which serve as a hole scavenger. The possible mechanism for the reaction is summarized in the Supporting Information. To prevent the recombination of electrons from the FTO to the oxidized species in the electrolyte, a thin TiO_2

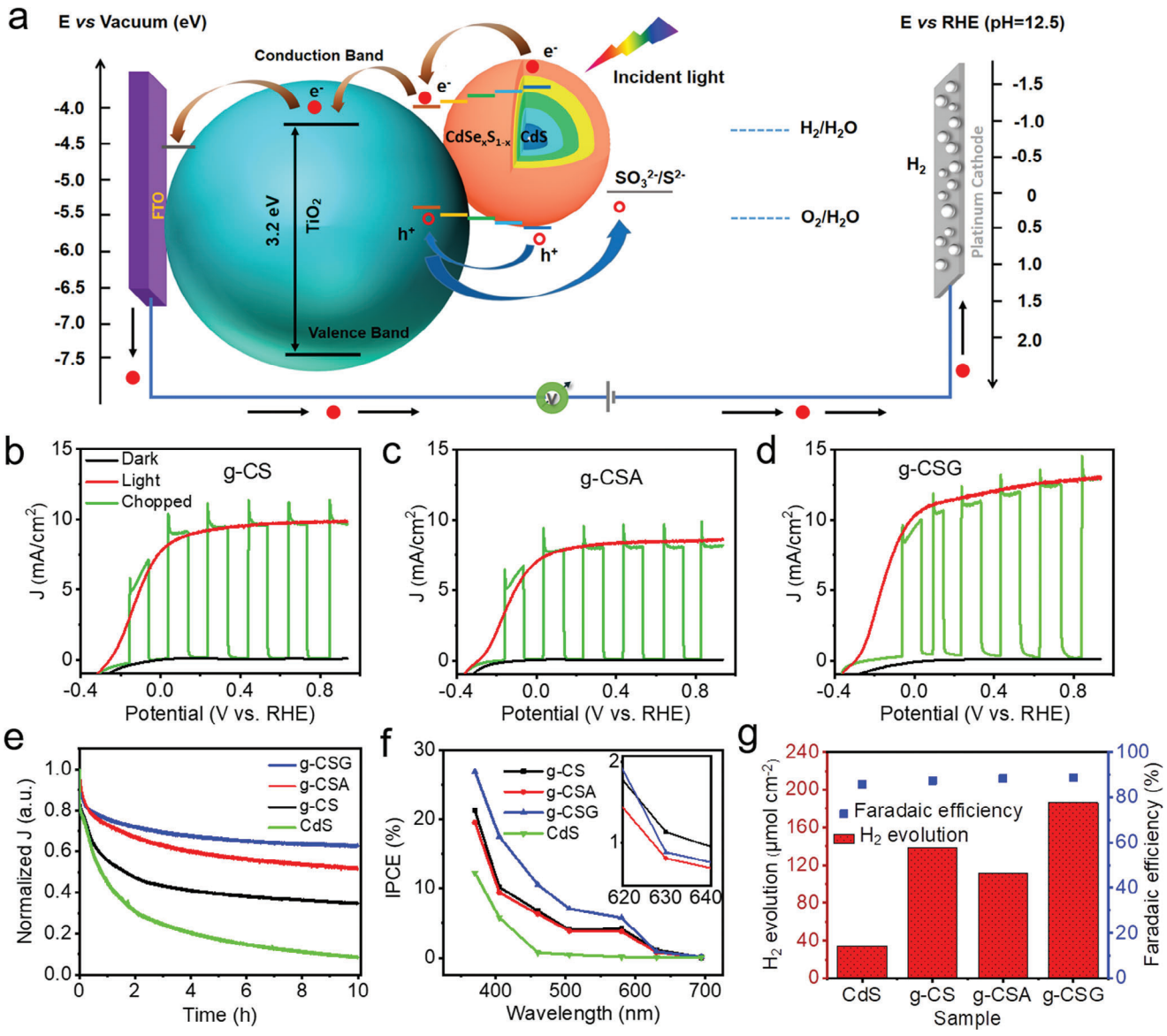

Figure 5. a) Schematic illustration of PEC device with carrier transfer, characteristic redox potentials, and electronic band alignment of g-CSG QDs sensitized TiO_2 anode. The arrows indicate the electrons and holes transfer processes. Photocurrent density (J, mA•cm^{-2}) versus potential (versus RHE) of PEC devices under dark (black line), chopped (green line) and continuous one sun light illumination (AM 1.5 G, 100 mW•cm^{-2}, red line): b) g-CS QDs; c) g-CSA QDs; d) g-CSG QDs. e) Comparison of normalized photocurrent density versus time curves of PEC devices based on CdS core QDs and the as-synthesized three different kinds of g-QDs sensitized TiO_2 at 0.6 V (versus RHE) under continuous one sun illumination. f) IPCE spectra of PEC devices based on CdS, g-CS, g-CSA and g-CSG QDs, respectively. g) H_2 production measurement of PEC cells based on CdS, g-CS, g-CSA, and g-CSG QDs, respectively. The measurements were conducted at 0.6 V versus RHE under continuous one-sun illumination (100 mW cm^{-2}, AM 1.5 G) for 1 h. The FE values (blue square) of the corresponding PEC devices are shown on the right vertical axis.

blocking layer was placed between the mesoporous TiO_2 and the FTO glass.

Compared to the structure of g-CS and g-CSA, the gradient layer in g-CSG QDs can serve as a "ladder" (gradual variation of energy level, as shown in Figure 1) for electrons and holes, improving the likelihood of electron transfer from the core to the shell region and extraction of the dissociated hole by the electrolyte. Meanwhile, the existence of a continuous gradient layer reduces the large potential at the sharp interface of CdS core and CdSe shell.[2] As a result, the undesirable carrier confinement originating from the lattice mismatch between CdS and CdSe in g-CSG QDs was reduced compared to that in g-CS and g-CSA QDs.

Figure 5b–d show the photocurrent density versus the applied voltage (vs RHE) curves of PEC devices assembled using our as-prepared QDs from g-CS, g-CSA, and g-CSG, respectively. A set of linear sweep voltammograms was conducted by using different photoanodes under dark (black curve) condition, light (red curve) condition and chopped one sun illumination (green curve) condition. Under the dark conditions, all curves show a

photocurrent density of approximately zero. All the light curves under one sun illumination condition (AM 1.5 G, 100 mW cm^{-2}) in Figure 5b–d demonstrate that the photocurrent density gradually increases with the increase of potential until a saturated current density is measured. For the chopped curves under discontinuous one-sun illumination (AM 1.5 G, 100 mW cm^{-2}), we can observe the real-time response of the photoanode upon illumination on and off, which is consistent with the variation trend of dark and light curves. The PEC cell fabricated with bare CdS QDs shows a saturated photocurrent density of 2.5 mA cm^{-2} (as shown in Figure S5, Supporting Information). The low photocurrent density is likely due to the limited absorption range in bare CdS QDs and the high density of traps on their surface. The latter act as non-radiative carrier recombination centers upon solar illumination. The saturated photocurrent density shows a noticeable enhancement for all PEC cells made with core/shell QDs. The PEC cell based on g-CS QDs presents a saturated current density of 9.8 mA cm^{-2}, as shown in Figure 5b. The g-CSA QDs based PEC cell shows a saturated current density of 8.5 mA cm^{-2} (Figure 5c), which is ≈13% lower than that of g-CS QDs. This is mainly attributed to the narrowing absorption limit toward shorter wavelengths, which can be observed from absorption spectra in Figure 3a. However, although g-CSG QDs also show a similar reduced absorption limit compared to g-CS QDs, the PEC devices based on the continuous gradient architecture g-CSG QDs reveal an outstanding ≈33.7% enhancement in saturated photocurrent density (up to 13.1 mA cm^{-2}, as observed in Figure 5d) compared to that of g-CS QDs, as well as a 54.1% improvement compared to that of g-CSA QDs. As mentioned above, the PL lifetime of g-CSA and g-CSG is higher than that of g-CS QDs, while the absorption range is lower than that of g-CS QDs. The results of the PEC measurement show that the g-CSG QDs exhibit enhanced performance compared to g-CS, and g-CSA QDs reveal reduced performance compared to g-CS. This behavior is because the PEC performance is affected by both the optical properties of QDs and the carrier dynamics in PEC cells. The latter will be discussed in detail in the carrier dynamics section. As summarized in Table S2 (Supporting Information), we compared the photocurrent density of PEC devices in this work with various state-of-the-art QDs reported in the literature. Under an identical configuration of the PEC cell, our work shows better performance with these state-of-the-art QDs-based PEC systems.

The long-term stability of the PEC device is also an essential factor toward commercializing this promising solar energy conversion technology. Stability measurements were conducted by recording the photocurrent density as a function of time for devices assembled using our as-prepared QDs respectively at 0.6 V versus RHE for 10 hours under continuous one-sun illumination (Figure 5e). The photocurrent densities for all kinds of QDs-based PEC cells gradually decrease during illumination. After 10 h light irradiation at 100 mW cm^{-2} intensity, the photocurrent densities maintain ≈ 62.8%, ≈ 51.9%, ≈ 34.8% and ≈ 8.6% of their initial value for PEC devices based on g-CSG, g-CSA, g-CS QDs, and CdS. The result shows that the g-QDs with continuous gradient shell structure can improve significantly the saturated current density and at the same time enhance the long-term stability of the PEC cell, taking advantage of the desirable electronic band alignment of the designed g-CSG QDs.

The long-term stability degradation may be due to the insufficient charge carrier separation/transfer dynamics in the QDs/TiO_2 system, as reported in previous work.[44] In addition, to further understand the possible reasons related to composition and chemical states in photoanodes for the degraded photocurrent density over time, we conducted XPS measurements to confirm the variation for the g-CSG QDs/TiO_2 photoanodes before and after two hours of stability test under continuous illumination. A high-resolution XPS spectrum of Cd 3d before the stability test is shown in Figure S6a (Supporting Information). The binding energies of Cd $3d_{3/2}$ and Cd $3d_{5/2}$ for g-CSG QDs/TiO_2 films are found at 411.9 and 405.1 eV, which are very close compared to the XPS analysis for g-CSG QDs in solution, reported in Figure 2g. This result suggests that the structure of QDs shows no significant change in the photoanode after EPD and before PEC stability measurements. Figure S6b (Supporting Information) shows the spectrum of Zn 2p before the stability test with a pair of peaks at 1022.2 and 1045.3 eV, which are consistent with the Zn $2p_{3/2}$ and $2p_{1/2}$ peaks from ZnS.[45] Figure S6 (Supporting Information) also shows that, after two hours of stability test, Cd 3d and Zn 2p peaks were observed with a significant shift of 0.5 and 0.7 eV toward lower binding energies. These peak shifts can probably be attributed to the partial surface oxidation of cadmium chalcogenide and ZnS in an alkaline electrolyte.[46] These results demonstrate that the long-term stability degradation observed in PEC devices could be attributed to the partly hole-induced self-oxidative decomposition of the surface metal chalcogenide (QDs and ZnS) due to the transient accumulation of photoexcited holes on the surface of the photoanode under illumination.

The g-CSA and g-CSG QDs have similar absorption ranges, which implies that the improvement in photocurrent density originates from shell's structural variation. As mentioned above, the continuous gradient $CdSe_xS_{1-x}$ structural layer in g-CSG QDs can minimize the interfacial lattice mismatch between the CdS core and $CdSe_xS_{1-x}$ gradient shell and also form several energy mid-gaps in the electronic band between the CdS core and CB of TiO_2, could reduce the undesirable carrier recombination and allow efficient electron transfer from the QDs to the TiO_2 film compared to the general core/shell g-CS or g-CSA QDs. The discrepancy of photocurrent densities in PEC devices based on core/shell g-QDs with different shell structures is affected by both electron transfer rates, electron lifetimes and impedance, which are discussed in the following section.

We measured the incident photon-to-current efficiency (IPCE) spectra of representative samples of PEC cells based on CdS QDs and different types of as-synthesized core/shell QDs. The IPCE is defined as the ratio of the number of collected photogenerated electrons by the electrodes and the number of incident monochromatic photons. A systematic comparison of the IPCE values for PEC cells based on CdS, g-CS, g-CSA and g-CSG QDs is shown in Figure 5f. The results demonstrate that PEC devices based on g-CSG QDs show clearly higher IPCE values in the visible region from 370 to 600 nm with respect to those based on CdS, g-CS and g-CSA QDs. This result is

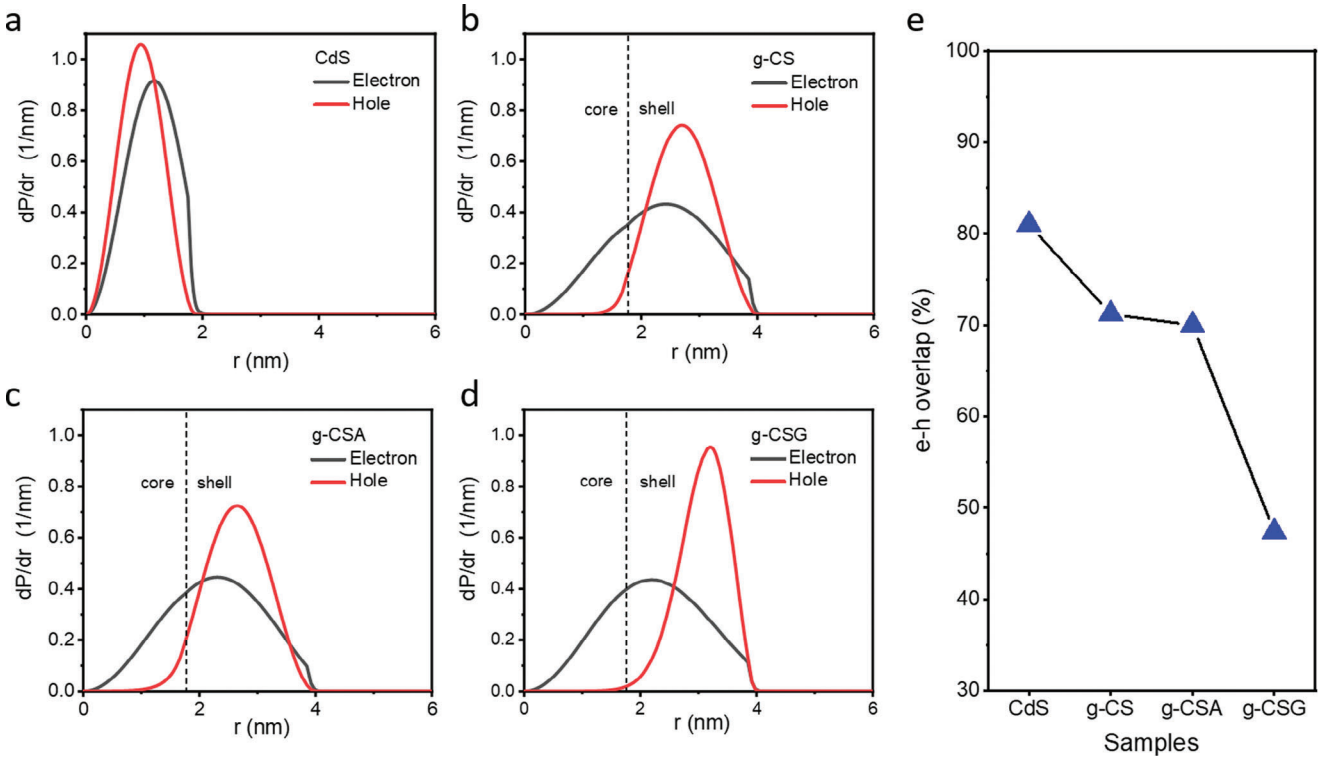

Figure 6. Theoretical simulation of different QDs. Spatial probability distribution dP/dr for the electron (black lines) and hole (red lines) states as a function of radius for a) CdS; b) g-CS; c) g-CSA; d) g-CSG, respectively. e) The electron and hole spatial overlap percentage for different QDs.

consistent with the differences in the obtained photocurrent density values.

To further confirm the conversion efficiency of the obtained photocurrent to H_2 evolution for PEC cells based on CdS and the as-synthesized core/shell QDs in our experiment, gas chromatography (GC) was employed to measure the amount of H_2 produced and calculate the Faradaic efficiency (FE) of the corresponding devices. As shown in Figure 5g, the PEC devices based on g-CSG QDs consistently show a higher amount of H_2 production (186.5 μmol cm^{-2}) during one hour of device operation and an average FE value of ≈ 88.7% compared to devices based on g-CS QDs (138.7 μmol cm^{-2} for H_2 production, ≈ 87.3% for FE) and g-CSA QDs (111.7 μmol cm^{-2} for H_2 production, ≈ 88.2% for FE). For CdS core QDs, the PEC devices only show a value of 34.2 μmol cm^{-2} of H_2 production and an average FE value of ≈ 85.8%. These results indicate that the obtained photocurrent in all these different samples is mainly attributed to H_2 production.

2.5. Theoretical Investigation

The theoretical electron and hole wave functions were calculated based on bulk band parameters by solving the time-independent Schrödinger equation in spherical geometry (see details in the Experimental Section and Figure S7, Supporting Information), to investigate electron and hole delocalization in CdS QDs and different core/shell g-QDs. The theoretical analysis of the spatial probability distribution value dP/dr of the electron and hole as a function of radius for different QDs is shown in **Figure 6**a–d and Figure S8 (Supporting Information), which demonstrate that the electrons and holes tend to preferentially delocalize into the shell region for all the core/shell g-QDs. As can be seen in Table S3 (Supporting Information), the calculated probability results show that more than 70% of electrons and 95% of holes delocalize into the shell region for all the core/shell g-QDs, which is consistent with a typical inverted type-I semiconductor nanostructure.

A systematic comparison of calculated electron and hole spatial overlap for CdS QDs and core/shell g-QDs with different shell structures is shown in Figure 6e and summarized in Table S4 (Supporting Information). The electron and hole spatial overlap is as high as 81.0% for bare CdS QDs. The large electron and hole spatial overlap indicates significant carrier recombination, which degrades the performance of PEC devices. The electron and hole spatial overlap decreases to 71.2% for g-CS QDs and 70.0% for g-CSA QDs due to their more pronounced leakage of holes, compared to electrons, into the shell region. The electron and hole spatial overlap is only 47.4% for g-CSG QDs, much lower compared to that for g-CS and g-CSA QDs. This result is mainly due to the significant displacement of the expected position for the holes, which leak to the outer part of the shell for g-CSG QDs (as shown in Figure S8b, Supporting Information). This can be attributed to the presence of a continuous gradient shell layer. The reduced electron and hole spatial overlap demonstrates an improved electron and hole spatial separation, which in turn decreases the probability of carrier recombination. This leads to a high photoexcited electron transfer efficiency when g-CSG QDs

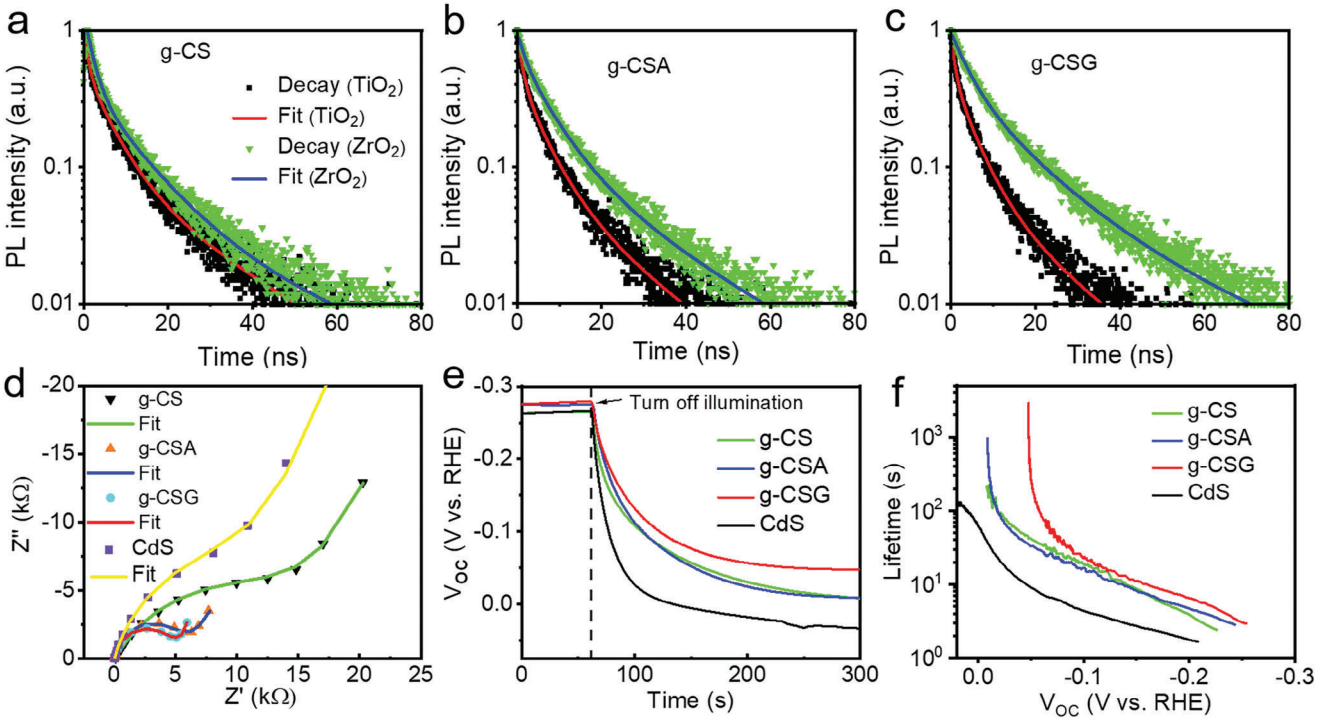

Figure 7. Comparison of the transient PL studies of a) g-CS, b) g-CSA, and c) g-CSG QDs coupled with TiO_2 and ZrO_2 mesoporous film. The excitation wavelength is set at λ_{ex} = 408 nm. d) Nyquist plots of PEC devices assembled using as-synthesized CdS, g-CS, g-CSA, and g-CSG QDs sensitized TiO_2 photoanodes at 0.55 V (vs RHE) applied bias in the three-electrode configuration under dark condition. The dots and solid lines represent the experimental data and fitting results, respectively. Transient photovoltage decay measurements of PEC devices based on CdS QDs and different g-QDs photoanodes: e) V_{oc} decay; f) electron lifetime calculated from the V_{oc} decay.

are employed as photon harvesters in PEC devices for H_2 production.

2.6. Carrier Dynamics Behavior

To better understand the obtained PEC performance, we investigated the carrier dynamics behavior (carrier transfer and carrier recombination) of the QDs/TiO_2 photoanode, in particular the electron transfer rates (k_{ET}), V_{oc} decay, electron lifetimes and electrochemical impedance properties. The efficiency of the photo-induced excitons separation and transfer was characterized via the electron transfer rate, which was calculated by measuring the lifetime of QDs anchored to TiO_2 and ZrO_2 mesoporous films. ZrO_2 was used as a benchmark where charge injection does not happen due to unfavorable electronic band alignment between QDs and ZrO_2. As a consequence, PL degradation could be attributed to the charge recombination inside the QDs. The k_{ET} can be calculated from the electron lifetime measurements for QDs coupled with TiO_2 and ZrO_2 mesoporous film using the following equation:

$$k_{ET} = \frac{1}{\tau\ (QDs/TiO_2)} - \frac{1}{\tau\ (QDs/ZrO_2)} \quad (3)$$

where $\tau\ (QDs/TiO_2)$ and $\tau\ (QDs/ZrO_2)$ are the average lifetime of QDs adhered to TiO_2 and ZrO_2 mesoporous films, respectively.

Figure 7a–c show typical transient PL measurements for all the QDs samples adhered to different mesoporous films. The lower k_{ET} of $(0.82 \pm 0.09) \times 10^7\ s^{-1}$ (shown in Figure S9, Supporting Information) for g-CS QDs can be attributed to the large interfacial potential at the sharp interface of CdS core and CdSe shell, which accelerates charge recombination at the core/shell interface.[2] In this case, charge carrier transfer was reduced due to the formation of interfacial defects as well as undesirable carrier confinement, which is a result of the lattice mismatch between CdS and CdSe (≈ 3.3%).[47] For g-CSA QDs, the k_{ET} value increases to $(1.61 \pm 0.11) \times 10^7\ s^{-1}$ because the introduction of an alloyed shell reduces the lattice mismatch in the core/shell system. The observation shows a more efficient electron transfer from CB of g-CSG QDs to that of TiO_2 in comparison to the other samples. The k_{ET} value of $(2.26 \pm 0.12) \times 10^7\ s^{-1}$ observed in the case of g-CSG is almost three-fold higher than g-CS QDs and 1.4 times higher than g-CSA QDs (shown in Figure S9, Supporting Information), making the former one suitable for charge separation in PEC cells. As a consequence, even though g-CS QDs show wider photo absorption compared to g-CSG QDs, the latter exhibit a higher saturated photocurrent density due to the advantage of a significantly improved transfer rate of electrons from the CB of TiO_2 mesoporous film to that of QDs. Meanwhile, even though g-CSA QDs show similar photo absorption compared to g-CSG QDs, the latter present an enhanced photocurrent density due to the higher electron transfer rate. Additionally, the reduced lattice mismatch in the gradient-designed g-CSG QDs is favorable for its high photocurrent density, which would significantly affect the performance of PEC cells.[2,48]

To further investigate the effect of different shell compositions and structures of the core/shell g-QDs on the charge transfer proprieties of the PEC devices, we conducted electrochemical impedance spectroscopy (EIS) measurements on CdS core QDs and three representative photoanodes based on the general CdSe shell of g-CS, alloyed $CdSe_{0.5}S_{0.5}$ shell of g-CSA and gradient $CdSe_xS_{1-x}$ shell of g-CSG under dark conditions. Figure 7d shows the Nyquist plots (Z″ vs Z′) for the different samples at an applied bias of 550 mV (vs RHE) and an AC voltage signal of 10 mV in amplitude. The results have been fitted according to the simple equivalent circuit shown in Figure S10 (Supporting Information), consisting of electrolyte solution resistance (R_s), charge transfer resistance (R_{ct}), constant phase element (CPE) and Warburg impedance (W). Approximate models have already been established to interpret the impedance spectra for similar systems.[49] In a typical Nyquist plot, one semicircle in the high-frequency region and one straight line in the low-frequency region can be observed, which is the expected behavior in the system containing electrolytes with solid electrodes.[50] Generally, semicircles observed in the high-frequency region can be attributed to the R_{ct} at the interface between the electrolyte and the semiconductor electrode, in which the diameter of the semicircle reflects the R_{ct}.[51] The fitting results (Figure S11, Supporting Information) show that the g-CSG sample exhibits the smallest R_{ct} value of 4.8 kΩ, which is smaller than the value of g-CSA (5.5 kΩ) and notably smaller than that of g-CS (16.8 kΩ). The R_{ct} of CdS QDs shows a larger value of 18.0 kΩ with respect to all the core/shell g-QDs. The higher R_{ct} value limits the charge transfer process at the photoanode and electrolyte interface, accelerating the charge recombination behavior inside QDs, which is not favorable for optoelectronic devices. On the contrary, the lower value of R_{ct} in the device based on g-CSG QDs leads to significant suppression of the recombination rate inside QDs. The main consequence of a lower recombination rate in the g-CSG QDs sample is an increased injection rate of electrons from the CB of QDs to that of TiO_2. As a result, the reduced R_{ct} in PEC cells based on g-CSG QDs could be an important factor in improving the photocurrent density in PEC cells. These results indicate that g-CSG QDs offer a more favorable energy band alignment for hole transfer to the electrolyte in PEC cells. As shown in Figure 5a, the photoexcited holes are absorbed by the electrolyte at the photoanode and electrolyte interface during PEC cells operation. Consequently, the hole leakage toward the surface of QDs can improve the efficiency of the hole transfer process after mixing QDs with a hole scavenger (Na_2S/Na_2SO_3). The reduced R_{ct} at the photoanode and electrolyte interface for g-CSG QDs is consistent with the abovementioned efficient hole leakage into the shell in g-CSG QDs, as discussed above in the theoretical investigation part. As the photoanodes were constructed in a similar way, the favorable kinetics charge transfer can be attributed to the release of the hole accumulation on the surface of g-CSG QDs due to the design of a unique gradient shell structure. The efficient hole transfer and release of the hole accumulation on the surface of g-CSG QDs reduce self-oxidation of QDs, as confirmed by XPS measurements and discussed above, explaining the reason for improved long-term stability in PEC cells based on g-CSG QDs with respect to their counterparts.[52]

To gain a deeper insight into the discrepancy of carrier transfer and carrier recombination at the TiO_2/QDs/electrolyte interface for the CdS core QDs and g-QDs with designed different shell structures, we performed transient photovoltage decay measurements to obtain the open-circuit voltage (V_{oc}) decay curves. The devices were illuminated under one sun simulated illumination until reaching a steady potential. The installation was maintained at the steady potential for 1 min, followed by shutting down the illumination. Subsequently, the voltage decay was recorded with time in dark conditions. Upon illumination, band gap excitation of QDs results in electrons/holes separation. The photoexcited electrons are injected into and accumulate within the CB of TiO_2, because photoexcited holes are scavenged by the electrolyte at the interface. The V_{oc} attains a steady state when there is an equilibration between the competition of electron accumulation and carrier recombination.[44] The illumination was then turned off, V_{oc} decays as the electrons accumulated within the TiO_2 undergo recombination with holes or are scavenged by oxidizing species from electrolyte (e.g., dissolved oxygen).[44,53] The representative V_{oc} decay curves for the PEC devices assembled using CdS core QDs and core/shell g-QDs with different shell compositions and structures are shown in Figure 7e, in which the PEC device based on g-CSG displays a significantly slower V_{oc} decay trend than the PEC devices based on CdS, g-CS and g-CSG QDs.

Monitoring the V_{oc} decay can also provide insights into the decay lifetime of the accumulated electrons, which can be related to the V_{oc} decay rate and derived using the following equation:[53]

$$\tau_e = \left(\frac{k_B T}{e}\right)\left(\frac{\mathrm{d}V_{oc}}{\mathrm{d}t}\right)^{-1} \quad (4)$$

where τ_e is the V_{oc} dependent electron lifetime, k_B is Boltzmann's constant, T is the temperature, e is the electron charge and V_{oc} is the open-circuit voltage at time t. The calculated electron lifetimes τ_e derived from Equation 4 as a function of V_{oc} for all PEC devices are presented in Figure 7f. The observation shows that τ_e values of the PEC devices based on g-CSG QDs are higher than that of the PEC devices based on CdS, g-CS and g-CSA QDs in all potential ranges of V_{oc}. In particular, the electron lifetime exhibits a significantly longer value in the lower V_{oc} range. For instance, at the potential of −0.05 V (vs RHE), the τ_e of the devices based on g-CSG QDs is ≈7 times longer compared to that of g-CSA QDs and ≈5 times longer compared to that of g-CS QDs.

All results presented here point to the beneficial role of the continuous gradient $CdSe_xS_{1-x}$ shell in enhancing the photocurrent density. The g-CSG sample yields a significantly improved electron transfer rate, prolonged electron lifetime, enhanced QY and suppression of the recombination rate as a result of its unique QD structure with continuous gradient $CdSe_xS_{1-x}$ shell layer incorporation. Such designed gradient shell layers in core/shell g-QDs are promising toward improving the performance of QDs-based PEC cells or other optoelectronic devices.

3. Conclusions and Perspectives

In conclusion, we performed a systematic comparative analysis for different types of core/shell QDs with varying shell structure and composition synthesized using an advanced interface engineering approach. Compared to g-CS and g-CSA QDs, the designed g-CSG QDs with an interfacial gradient shell smooth the

sharp core-shell interface and allow reduced interfacial strain by minimizing the lattice mismatch between core and shell. Optical characterization demonstrates that both g-CSA and g-CSG QDs exhibit a blue-shift absorption and PL response to shorter wavelengths compared to g-CS QDs. We obtained a high saturated photocurrent density of 13.1 mA cm^{-2} under one sun illumination for PEC cells based on g-CSG QDs with the continuous gradient architecture shell layer, enhancing by ≈54.1% and ≈33.7% compared to that of g-CSA and g-CS QDs, respectively. Additionally, theoretical simulation and carrier dynamics measurements highlight that the incorporation of continuous gradient $CdSe_xS_{1-x}$ shell in g-CSG QDs significantly decreases the electron/hole spatial overlap, improves the electron transfer rate, prolongs electron lifetime and enhances the charge transfer at the QDs/electrolyte interface. As a result, despite the slight reduction in absorption range, the gradient shell in g-CSG QDs allows for higher photocurrent density. The results demonstrate that the designed g-CSG QDs hold great potential for applications in QDs-based PEC cells. This work also highlights how interface engineering in core/shell g-QDs offers an effective strategy to optimize optoelectronic properties and pave the way for designing and modifying optical and electronic properties of other heterostructured g-QDs for application in solar technologies. Future work will focus on the interface engineering of eco-friendly core/shell QDs (such as InP/ZnSe, $AgInSe_2/AgInS_2$, CuInSeS/ZnS, etc.) by optimizing the composition/thickness of interfacial layers or designing appropriate gradients to enable efficient charge transfer and further realize high-efficiency in optoelectronic devices based on core/shell g-QDs.

4. Experimental Section

Materials, synthesis of CdS QDs, synthesis of core/shell g-QDs, TiO_2 film preparation, ZrO_2 film preparation, deposition of the as-synthesized QDs into the TiO_2 mesoporous films, QDs/ZrO_2 film preparation, and characterization, can be found in Supporting Information.

Supporting Information

Supporting Information is available from the Wiley Online Library or from the author.

Acknowledgements

F.R. and S.S. acknowledge NSERC for funding through individual Discovery Grants and the Canada Foundation for Innovation (CFI) for infrastructure and its operating funds. F.R. is also grateful to the Canada Research Chairs program for funding and partial salary support. H.Z. acknowledges his doctoral Excellence Scholarship from the UNESCO Chair MATECSS and the Fonds de recherche du Québec Nature et technologies (FRQNT) for a Ph.D. Fellowship. G.S.S. acknowledges NSERC for funding through an individual Discovery Grant. This work was supported by the National Natural Science Foundation of China (52202294) and the Fundamental Research Funds for the Central Universities (XJS221403).

Conflict of Interest

The authors declare no conflict of interest.

Data Availability Statement

The data that support the findings of this study are available from the corresponding author upon reasonable request.

Keywords

carrier dynamics, hydrogen evolution, interface engineering, quantum dots, theoretical calculation

Received: July 22, 2023
Revised: November 19, 2023
Published online: December 21, 2023

[1] a) X. Dai, Y. Deng, X. Peng, Y. Jin, *Adv. Mater.* **2017**, *29*, 1607022; b) S. M. Tenney, V. Vilchez, M. L. Sonnleitner, C. Huang, H. C. Friedman, A. J. Shin, T. L. Atallah, A. P. Deshmukh, S. Ithurria, J. R. Caram, *J. Phys. Chem. Lett.* **2020**, *11*, 3473; c) X. Zhang, H. Xie, Z. Liu, C. Tan, Z. Luo, H. Li, J. Lin, L. Sun, W. Chen, Z. Xu, L. Xie, W. Huang, H. Zhang, *Angew. Chem., Int. Ed.* **2015**, *54*, 3653; d) S. Chan, M. Liu, K. Latham, M. Haruta, H. Kurata, T. Teranishi, Y. Tachibana, *J. Mater. Chem. C* **2017**, *5*, 2182; e) J. Engel, S. R. Bishop, L. Vayssieres, H. L. Tuller, *Adv. Funct. Mater.* **2014**, *24*, 4952; f) O. Abdelkarim, G. S. Selopal, K. Suresh, F. Navarro-Pardo, P. Kumar, K. K. Ghuman, A. Yurtsever, G. Bassioni, Z. M. Wang, F. Rosei, *Chem. Eng. J.* **2022**, *429*, 132425.

[2] G. S. Selopal, H. Zhao, G. Liu, H. Zhang, X. Tong, K. Wang, J. Tang, X. Sun, S. Sun, F. Vidal, Y. Wang, Z. M. Wang, F. Rosei, *Nano Energy* **2019**, *55*, 377.

[3] a) L. Gao, L. N. Quan, F. P. García De Arquer, Y. Zhao, R. Munir, A. Proppe, R. Quintero-Bermudez, C. Zou, Z. Yang, M. I. Saidaminov, O. Voznyy, S. Kinge, Z. Lu, S. O. Kelley, A. Amassian, J. Tang, E. H. Sargent, *Nat. Photonics* **2020**, *14*, 227; b) B. N. Pal, Y. Ghosh, S. Brovelli, R. Laocharoensuk, V. I. Klimov, J. A. Hollingsworth, H. Htoon, *Nano Lett.* **2012**, *12*, 331.

[4] G. Konstantatos, I. Howard, A. Fischer, S. Hoogland, J. Clifford, E. Klem, L. Levina, E. H. Sargent, *Nature* **2006**, *442*, 180.

[5] a) H. Zhao, A. Vomiero, F. Rosei, *Small* **2015**, *11*, 5741; b) J. Liu, H. Zhang, G. S. Selopal, S. Sun, H. Zhao, F. Rosei, *ACS Photonics* **2019**, *6*, 2479.

[6] M. Frasco, N. Chaniotakis, *Sensors* **2009**, *9*, 7266.

[7] a) H. Zhao, R. Sun, Z. Wang, K. Fu, X. Hu, Y. Zhang, *Adv. Funct. Mater.* **2019**, *29*, 1902262; b) H. Zhao, D. Benetti, X. Tong, H. Zhang, Y. Zhou, G. Liu, D. Ma, S. Sun, Z. M. Wang, Y. Wang, F. Rosei, *Nano Energy* **2018**, *50*, 756.

[8] a) H. Zhao, H. Zhang, G. Liu, X. Tong, J. Liu, G. S. Selopal, Y. Wang, Z. M. Wang, S. Sun, F. Rosei, *Appl. Catal., B* **2019**, *250*, 234; b) H. Zhang, L. V. Besteiro, J. Liu, C. Wang, G. S. Selopal, Z. Chen, D. Barba, Z. M. Wang, H. Zhao, G. P. Lopinski, S. Sun, F. Rosei, *Nano Energy* **2021**, *79*, 105416; c) H. Zhao, X. Li, M. Cai, C. Liu, Y. You, R. Wang, A. I. Channa, F. Lin, D. Huo, G. Xu, X. Tong, Z. M. Wang, *Adv. Energy Mater.* **2021**, *11*, 2101230; d) B. Luo, J. Liu, H. Guo, X. Liu, R. Song, K. Shen, Z. M. Wang, D. Jing, G. S. Selopal, F. Rosei, *Nano Energy* **2021**, *88*, 106220; e) O. Abdelkarim, A. Mirzaei, G. S. Selopal, A. Yurtsever, G. Bassioni, Z. M. Wang, M. Chaker, F. Rosei, *Chem. Eng. J.* **2022**, *446*, 137312.

[9] H. Zhao, F. Rosei, *Chem* **2017**, *3*, 229.

[10] A. Fujishima, K. Honda, *Nature* **1972**, *238*, 37.

[11] M. Grätzel, *Nature* **2001**, *414*, 338.

[12] I. S. Cho, Z. Chen, A. J. Forman, D. R. Kim, P. M. Rao, T. F. Jaramillo, X. Zheng, *Nano Lett.* **2011**, *11*, 4978.

[13] a) S. K. Mohapatra, M. Misra, V. K. Mahajan, K. S. Raja, *J. Phys. Chem. C* **2007**, *111*, 8677; b) M. Mohammadnezhad, G. S. Selopal, O. Cavuslar, D. Barba, E. G. Durmusoglu, H. Y. Acar, Z. M. Wang, G.

P. Lopinski, B. Stansfield, H. Zhao, F. Rosei, *Chem. Eng. J.* **2021**, *421*, 127756.
[14] a) M. Liu, N. De Leon Snapp, H. Park, *Chem. Sci.* **2011**, *2*, 80; b) G. Wang, H. Wang, Y. Ling, Y. Tang, X. Yang, R. C. Fitzmorris, C. Wang, J. Z. Zhang, Y. Li, *Nano Lett.* **2011**, *11*, 3026.
[15] R. Akilimali, G. S. Selopal, M. Mohammadnezhad, I. Ka, Z. M. Wang, G. P. Lopinski, H. Zhao, F. Rosei, *Chem. Eng. J.* **2022**, *435*, 135037.
[16] U. Bach, D. Lupo, P. Comte, J. E. Moser, F. Weissörtel, J. Salbeck, H. Spreitzer, M. Grätzel, *Nature* **1998**, *395*, 583.
[17] N. Yang, Y. Liu, H. Wen, Z. Tang, H. Zhao, Y. Li, D. Wang, *ACS Nano* **2013**, *7*, 1504.
[18] H. Zhang, G. S. Selopal, Y. Zhou, X. Tong, D. Benetti, L. Jin, F. Navarro-Pardo, Z. Wang, S. Sun, H. Zhao, F. Rosei, *Nanoscale* **2017**, *9*, 16843.
[19] R. Adhikari, L. Jin, F. Navarro-Pardo, D. Benetti, B. Alotaibi, S. Vanka, H. Zhao, Z. Mi, A. Vomiero, F. Rosei, *Nano Energy* **2016**, *27*, 265.
[20] X. Tong, X.-T. Kong, C. Wang, Y. Zhou, F. Navarro-Pardo, D. Barba, D. Ma, S. Sun, A. O. Govorov, H. Zhao, Z. M. Wang, F. Rosei, *Adv. Sci.* **2018**, *5*, 1800656.
[21] D. C. Lee, I. Robel, J. M. Pietryga, V. I. Klimov, *J. Am. Chem. Soc.* **2010**, *132*, 9960.
[22] C. Wang, D. Barba, G. S. Selopal, H. Zhao, J. Liu, H. Zhang, S. Sun, F. Rosei, *Adv. Funct. Mater.* **2019**, *29*, 1904501.
[23] a) H. Zhang, J. Liu, C. Wang, G. S. Selopal, D. Barba, Z. M. Wang, S. Sun, H. Zhao, F. Rosei, *ACS Photonics* **2019**, *6*, 2421; b) S. Zou, Y. Liu, J. Li, C. Liu, R. Feng, F. Jiang, Y. Li, J. Song, H. Zeng, M. Hong, X. Chen, *J. Am. Chem. Soc.* **2017**, *139*, 11443; c) R. Beaulac, P. I. Archer, S. T. Ochsenbein, D. R. Gamelin, *Adv. Funct. Mater.* **2008**, *18*, 3873; d) C. S. Erickson, L. R. Bradshaw, S. Mcdowall, J. D. Gilbertson, D. R. Gamelin, D. L. Patrick, *ACS Nano* **2014**, *8*, 3461.
[24] E. G. Durmusoglu, G. S. Selopal, M. Mohammadnezhad, H. Zhang, P. Dagtepe, D. Barba, S. Sun, H. Zhao, H. Y. Acar, Z. M. Wang, F. Rosei, *ACS Appl. Mater. Interfaces* **2020**, *12*, 36301.
[25] a) I. Coropceanu, M. G. Bawendi, *Nano Lett.* **2014**, *14*, 4097; b) S. A. Ivanov, A. Piryatinski, J. Nanda, S. Tretiak, K. R. Zavadil, W. O. Wallace, D. Werder, V. I. Klimov, *J. Am. Chem. Soc.* **2007**, *129*, 11708; c) H. Zhao, G. Liu, F. Vidal, Y. Wang, A. Vomiero, *Nano Energy* **2018**, *53*, 116.
[26] Z. Li, A. I. Channa, Z. M. Wang, X. Tong, *Small n/a*, 2305146.
[27] a) H. Guo, B. Luo, J. Wang, B. Wang, X. Huang, J. Yang, W. Gong, Y. Zhou, X. Niu, *J. Mater. Chem. A* **2020**, *8*, 24655; b) H. Guo, P. Yang, J. Hu, A. Jiang, H. Chen, X. Niu, Y. Zhou, *ACS Omega* **2022**, *7*, 9642.
[28] S. Jiao, J. Wang, Q. Shen, Y. Li, X. Zhong, *J. Mater. Chem. A* **2016**, *4*, 7214.
[29] a) Y.-S. Park, J. Lim, V. I. Klimov, *Nat. Mater.* **2019**, *18*, 249; b) J. Lim, Y.-S. Park, V. I. Klimov, *Nat. Mater.* **2018**, *17*, 42; c) W. K. Bae, Y.-S. Park, J. Lim, D. Lee, L. A. Padilha, H. Mcdaniel, I. Robel, C. Lee, J. M. Pietryga, V. I. Klimov, *Nat. Commun.* **2013**, *4*, 2661; d) W. K. Bae, L. A. Padilha, Y.-S. Park, H. Mcdaniel, I. Robel, J. M. Pietryga, V. I. Klimov, *ACS Nano* **2013**, *7*, 3411.
[30] W. Nan, Y. Niu, H. Qin, F. Cui, Y. Yang, R. Lai, W. Lin, X. Peng, *J. Am. Chem. Soc.* **2012**, *134*, 19685.
[31] G. Liu, W. Liang, X. Xue, F. Rosei, Y. Wang, *Adv. Sci.* **2021**, *8*, 2102784.
[32] J. Hou, H. Zhao, F. Huang, Q. Jing, H. Cao, Q. Wu, S. Peng, G. Cao, *J. Power Sources* **2016**, *325*, 438.
[33] L. Zhao, J. Jia, Z. Yang, J. Yu, A. Wang, Y. Sang, W. Zhou, H. Liu, *Appl. Catal., B* **2017**, *210*, 290.
[34] J.-J. Wang, Y.-Q. Wang, F.-F. Cao, Y.-G. Guo, L.-J. Wan, *J. Am. Chem. Soc.* **2010**, *132*, 12218.
[35] O. Labeau, P. Tamarat, B. Lounis, *Phys. Rev. Lett.* **2003**, *90*, 257404.
[36] H. Zhao, Z. Fan, H. Liang, G. S. Selopal, B. A. Gonfa, L. Jin, A. Soudi, D. Cui, F. Enrichi, M. M. Natile, I. Concina, D. Ma, A. O. Govorov, F. Rosei, A. Vomiero, *Nanoscale* **2014**, *6*, 7004.
[37] a) J. Zhang, X. Zhang, J. Y. Zhang, *J. Phys. Chem. C* **2010**, *114*, 3904; b) M. G. Bawendi, P. J. Carroll, W. L. Wilson, L. E. Brus, *J. Chem. Phys.* **1992**, *96*, 946.
[38] M. Jones, S. S. Lo, G. D. Scholes, *Proc. Natl. Acad. Sci. USA* **2009**, *106*, 3011.
[39] H. Zhang, Y. Ye, J. Zhang, Y. Cui, B. Yang, L. Shen, *J. Phys. Chem. C* **2012**, *116*, 15660.
[40] C. J. Hanson, N. F. Hartmann, A. Singh, X. Ma, W. J. I. Debenedetti, J. L. Casson, J. K. Grey, Y. J. Chabal, A. V. Malko, M. Sykora, A. Piryatinski, H. Htoon, J. A. Hollingsworth, *J. Am. Chem. Soc.* **2017**, *139*, 11081.
[41] a) O. Stroyuk, A. Raevskaya, N. Gaponik, O. Selyshchev, V. Dzhagan, S. Schulze, D. R. T. Zahn, *J. Phys. Chem. C* **2018**, *122*, 10267; b) N. Mahapatra, S. Panja, A. Mandal, M. Halder, *J. Mater. Chem. C* **2014**, *2*, 7373; c) Z. Wang, X. Xing, Y. Yang, R. Zhao, T. Zou, Z. Wang, Y. Wang, *Sci. Rep.* **2018**, *8*, 8953.
[42] K. Wang, Y. Tao, Z. Tang, D. Benetti, F. Vidal, H. Zhao, F. Rosei, X. Sun, *Nano Energy* **2022**, *100*, 107524.
[43] J. Tang, K. W. Kemp, S. Hoogland, K. S. Jeong, H. Liu, L. Levina, M. Furukawa, X. Wang, R. Debnath, D. Cha, K. W. Chou, A. Fischer, A. Amassian, J. B. Asbury, E. H. Sargent, *Nat. Mater.* **2011**, *10*, 765.
[44] G. S. Selopal, M. Mohammadnezhad, F. Navarro-Pardo, F. Vidal, H. Zhao, Z. M. Wang, F. Rosei, *Nanoscale Horiz.* **2019**, *4*, 404.
[45] B. Liu, X. Hu, X. Li, Y. Li, C. Chen, K.-H. Lam, *Sci. Rep.* **2017**, *7*, 16396.
[46] a) K. S. Ranjith, A. Senthamizhan, B. Balusamy, T. Uyar, *Catal. Sci. Technol.* **2017**, *7*, 1167; b) S. Majumder, A. C. Mendhe, D. Kim, B. R. Sankapal, *J. Alloys Compd.* **2019**, *788*, 75.
[47] B. G. Jeong, Y.-S. Park, J. H. Chang, I. Cho, J. K. Kim, H. Kim, K. Char, J. Cho, V. I. Klimov, P. Park, D. C. Lee, W. K. Bae, *ACS Nano* **2016**, *10*, 9297.
[48] G. S. Selopal, O. Abdelkarim, P. Kumar, L. Jin, J. Liu, H. Zhao, A. Yurtsever, F. Vidal, Z. M. Wang, F. Rosei, *ACS Appl. Energy Mater.* **2022**, *5*, 1447.
[49] a) J. Bisquert, G. Garcia-Belmonte, P. Bueno, E. Longo, L. O. S. Bulhões, *J. Electroanal. Chem.* **1998**, *452*, 229; b) T.-T. Gu, X.-M. Wu, Y.-M. Dong, G.-L. Wang, *J. Electroanal. Chem.* **2015**, *759*, 27; c) X. Wang, T. Yan, Y. Li, Y. Liu, B. Du, H. Ma, Q. Wei, *Sci. Rep.* **2015**, *5*, 17945; d) K. Ozoemena, *Sensors* **2006**, *6*, 874.
[50] A. J. Peltekoff, V. E. Hiller, G. P. Lopinski, O. A. Melville, B. H. Lessard, *ACS Applied Polymer Materials* **2019**, *1*, 3210.
[51] H. Zhang, X. Liu, R. Wang, R. Mi, S. Li, Y. Cui, Y. Deng, J. Mei, H. Liu, *J. Power Sources* **2015**, *274*, 1063.
[52] R. Adhikari, K. Basu, Y. Zhou, F. Vetrone, D. Ma, S. Sun, F. Vidal, H. Zhao, F. Rosei, *J. Mater. Chem. A* **2018**, *6*, 6822.
[53] B. H. Meekins, P. V. Kamat, *ACS Nano* **2009**, *3*, 3437.